



# 1 **Modeling CMAQ dry deposition treatment over Western Pacific: A** 2 **distinct characteristic of mineral dust and anthropogenic aerosol**

3 Steven Soon-Kai Kong<sup>1</sup>, Joshua S. Fu<sup>2</sup>, Neng-Huei Lin<sup>1,3,\*</sup>, Guey-Rong Sheu<sup>1,3,\*</sup>, Wei-Syun Huang<sup>1</sup>

4  
5 <sup>1</sup> Department of Atmospheric Sciences, National Central University, Taoyuan, 32001, Taiwan

6 <sup>2</sup> Department of Civil and Environmental Engineering, the University of Tennessee Knoxville, TN37996,  
7 USA

8 <sup>3</sup> Center for Environmental Monitoring and Technology, National Central University, Taoyuan, 32001,  
9 Taiwan

10 *Correspondence to:* Neng-Huei Lin ([nhlin@cc.ncu.edu.tw](mailto:nhlin@cc.ncu.edu.tw)) and Guey-Rong Sheu  
11 ([grsheu@atm.ncu.edu.tw](mailto:grsheu@atm.ncu.edu.tw))

12 **Abstract.** Dry deposition plays a vital role in the aerosol removal process from the atmosphere. However,  
13 the chemical transport model (CTM) is sensitive to the dry deposition parameterization and yet remains  
14 to be determined due to the limited particle deposition measurement. By utilizing the CMAQv5.4 with  
15 the refined dust emission treatment (Kong et al., 2024), the East Asian dust (EAD) simulation during  
16 January 2023 was constructed to evaluate the performance of dry deposition parameterizations developed  
17 by PR11 (Pleim and Ran, 2011), E20 (Emerson et al., 2020), S22 (Shu et al., 2022) and P20 (Pleim et al.,  
18 2022), respectively. The result showed that the dry deposition parameterization could significantly  
19 improve the CMAQ dust emission treatment. By implementing the E20 dry deposition scheme, the  
20 CMAQ simulation performance of the surface PM<sub>10</sub> has been considerably improved with the NMB of -  
21 41.9 %, as compared to the dry deposition proposed by PR11 (54.05 %), S22 (-47.01 %) and P22 (-53.90  
22 %). The modeled PM<sub>10</sub> pattern by E20 at the upper level (700 hPa) was mostly consistent with the  
23 observed PM<sub>10</sub> at the Lulin Atmospheric Background Station (LABS; 23.47° N, 120.87° E; 2862 m a.s.l.)  
24 where is a typical background site at Western Pacific, particularly in capturing the peak value. The high-  
25 altitude correlations (R) were well performed for E20 by 0.55, as compared to PR11 (0.47), S22 (0.54)  
26 and P22 (0.46). Moreover, E20 improved the simulated aerosol optical depth (AOD) value during the  
27 multiple dust storm in spring 2021. The noticeable reduction of the coarse mode particle's deposition  
28 velocity ( $V_d$ ) was responsible for resolving the PM<sub>10</sub> simulation underestimation. Moreover, the  
29 significant improvement of PM<sub>10</sub> was also shown by the modeled PM<sub>2.5</sub>. On 22-31 January 2023, the *in-*  
30 *situ* measurement of the upper level observed the possibility of natural dust and anthropogenic aerosol.



31 This is consistent with the CMAQ, which shows that both aerosol types displayed a clear "long dust-black  
32 carbon belt" along the 15°N. We proposed implementing the E20 dry deposition approach, resolving the  
33 uncertainty of the CMAQ dust emission treatment.

## 34 **1 Introduction**

35 The chemical transport model (CTM) is a powerful tool for comprehending air pollution, encompassing  
36 emission, transport, radiative impact, and removal mechanisms at various grid scales. Among  
37 these, particle dry deposition, a crucial aerosol removal process, exerts a significant influence on the  
38 physical and chemical aerosol properties, meteorological impact, terrain, and vegetation. The derivation  
39 of the dry deposition is based on the resistance framework and electrical analogue, but its implementation  
40 can vary across models (Wesley, 1989; Giardina and Buffa, 2018; Gaydos et al., 2007; Khan and  
41 Perlinger, 2017; Shu et al., 2017). A key challenge in dry deposition simulation is the scarcity of  
42 measurement data for model verification, underscoring the necessity for further research to enhance the  
43 accuracy of air quality modeling.

44 An immense range of dry deposition parameterization has been implanted in the model. The  
45 deposition mechanism by Slinn (1982) includes the deposition process such as turbulent transfer,  
46 Brownian diffusion, impaction, interception, gravitational settling, and particle rebound, where the  
47 particle grows under humid conditions. Zhang et al. (2001) suggested the dry deposition scheme is  
48 sensitive to land use category and several parameters. For instance, due to the particle growth, the  
49 deposition velocity ( $V_d$ ) over the ocean is much higher than on another land surface, as the  $V_d$  increased  
50 rapidly with the increase of particle size. However, Zhang et al. (2001) parameterization still  
51 underestimated the global  $PM_{2.5}$  concentration. The latest dry deposition scheme revision by Emerson et  
52 al. (2020) has resolved the problem, marking a significant step forward in our quest for more accurate air  
53 quality modeling.

54 An updated deposition scheme that reduces the dependence of the deposition velocity on the aerosol  
55 mode width has been proposed (Shu et al., 2022). Indeed, the approach suggested that vegetation  
56 dependence increased the  $V_d$  for submicrons and decreased for large particles by 37 % and -66 %,



57 respectively. It also reduced the functional biases by 56-97 % for vegetated land-use type and equivalence  
58 performance over the water. Moreover, adding the second inertial impaction term for microscale obstacles  
59 such as leaf hairs, microscale ridges, and needle leaf edge effects managed to increase the mass dry  
60 deposition of the accumulation mode aerosols in the model (Pleim et al., 2022). These modifications  
61 reduced the averaged  $PM_{2.5}$  in the atmosphere during July 2018 over the contiguous United States.

62 With a plethora of deposition approaches in use, it becomes paramount to comprehend their impact  
63 on model performance in predicting aerosol behavior. The surface fine particle concentrations can vary  
64 by 5-15 % due to the different dry deposition schemes, with the boarder extending by more than 200 %  
65 of particle dry deposition due to the different algorithms (Saylor et al., 2019). A comprehensive evaluation  
66 of five different parameterizations has been conducted, with the simplest and most effective deposition  
67 mechanism suggested for the CTM (Khan and Perlinger, 2017). However, the model's reliance on  
68 meteorological factors such as frictional velocity, relative humidity, rainfall, or wind speed, which can  
69 significantly influence the model's accuracy, remains a challenge (Kong et al., 2021).

70 Besides the model bias on  $PM_{2.5}$ , the simulation of  $PM_{10}$  has been underestimated by the deposition  
71 mechanism, as the coarse mode has been generally represented, particularly over the western Pacific  
72 (Kong et al., 2021). The  $V_d$  is overestimated for coarse particles, where the dry deposition velocity is too  
73 high for coarse particles when the frictional velocity is large, which is why the surface  $PM_{10}$  concentration  
74 is underestimated (Ryu and Min, 2022). The model performance of  $PM_{10}$  simulation that is widely  
75 influenced by the dust treatment embedded within CMAQ has been revised (Dong et al., 2016; Liu et al.,  
76 2021; Kong et al., 2021, 2024) and are found to effectively simulate the  $PM_{10}$  over the western Pacific  
77 region such as Taiwan. However, the issue regarding the deposition algorithm's impact on the model  
78 performance at the corresponding region needs to be discussed. The present research intends to evaluate  
79 the CMAQ model performance due to the different deposition schemes on aerosols in the Taiwan region.

80 The model performance in Taiwan is of paramount importance in our study, as the area is equipped with  
81 a substantial number of well-maintained surface observation sites, providing comprehensive coverage.  
82 Additionally, the LABS station, located in the high-altitude subtropical western North Pacific region,



83 serves as the sole background station for monitoring transboundary pollutants, further underscoring the  
84 relevance of our research.

## 85 **2 Data and Methodology**

### 86 **2.1 Dust emission treatment**

87 Before delving into the details, it's important to understand the process of dust transport. Dust is primarily  
88 transported by wind through a process known as sandblasting (Kok et al., 2012). For dust to be uplifted,  
89 the horizontal wind speed must exceed a certain threshold frictional velocity ( $u_{*,t}$ ), which is estimated by  
90 the model as follows:

$$91 \quad u_{*,t} = u_{*,to} f_m f_r \quad (1)$$

92 where  $f_m$  and  $f_r$  are the correction factors of soil moisture and surface roughness, respectively, and  $u_{*,to}$   
93 is the ideal threshold friction velocity.

94 Through a collaborative effort, the windspeed, soil texture, soil moisture, and surface roughness  
95 length derived from field and laboratory studies have been integrated into the windblown dust treatment,  
96 which is now a part of the Community Multiscale Air Quality (CMAQ) modeling system (Foroutan et  
97 al., 2017). This model, developed and evaluated over the continental United States, has also been extended  
98 to the East Asia region (Dong et al., 2016; Liu et al., 2021; Kong et al., 2021, 2024). Kong et al. (2024)  
99 have proposed further improvements, including the integration of the revised soil moisture fraction, dust  
100 emission speciation profile, and bulb soil density, to enhance the representation of the Asian dust  
101 simulation. This ongoing collaboration is crucial for the continuous improvement of our understanding  
102 and management of dust emissions.

### 103 **2.2 Particle dry deposition schemes**

104 Particle dry deposition is a complex process relating to the deposition velocity, particle size, source and  
105 composition, land use surface, and meteorological condition. Generally, the flux of the particle mass  
106 through the surface boundary layer is estimated as:



107  $F = C \times V_d$  (2)

108 where  $F$  is the deposition flux,  $C$  is the particle concentration at the surface layer, and  $V_d$  is the deposition  
109 velocity.

110 The difference in the particle concentration and deposition prediction among the various  
111 atmospheric chemistry models was probably due to the algorithm of the dry deposition particle. The  
112 algorithm describing particle deposition velocity as a function of particle size in almost all current air  
113 quality model systems is descended from (Slinn, 1982). The particle deposition according to vegetative  
114 canopies formulated the deposition velocity as:

115  $V_d = V_g + \frac{1}{R_a + R_s}$  (3)

116 where  $V_s$  is the gravitation settling velocity,  $R_a$  is the resistivity aerodynamic and  $R_s$  is the surface  
117 resistivity. The  $V_s$  is calculated according to Stokes's Law as:

118  $V_g = V_s + \frac{\rho_p D_p^2 g C_c}{18\eta}$  (4)

119 where,  $\rho_p$  is the density of the particle;  $D_p$  is the diameter of the particle;  $g$  is gravitational acceleration;  
120  $C_c$  is the Cunningham correction factor for small particles; and,  $\eta$  is the dynamic viscosity of air.

121 CMAQ implemented the dry deposition scheme that Pleim and Ran (2011) proposed based on  
122 Slinn (1982), as shown in Table 1. Dry deposition is based on gravitational settling velocity ( $V_g$ ), which  
123 is the function of aerodynamic and surface resistance. According to Pleim and Ran (2011), chemical  
124 surface flux modeling has become an essential process in the air quality model. For instance, the linkages  
125 of ambient concentration levels to the deposition of  $SO_x$  and  $NO_x$ . The algorithm has been applied in  
126 CMAQv4.5 up to CMAQv5.4. In CMAQv5.4, Surface Tiled Aerosol and Gaseous Exchange (STAGE)  
127 deposition has been implemented within the model, where estimated fluxes from sub-grid cell fractional  
128 land-use values, aggregates the fluxes to the model grid cell and unifies the bidirectional and



129 unidirectional deposition schemes using the resistance framework (Massad et al., 2010; Nemitz et al.,  
130 2001).

### 131 **2.3 CMAQ model design**

132 This study applied WRF v4.0 for the meteorological field parameters and CMAQv5.4 to simulate the  
133 transboundary East Asian dust episodes on 22-31 January 2023, and the three dust storm episodes on 14-  
134 16 March 2021, 26-28 March 2021 and 17-19 April 2021. The modeling domain was set up to cover the  
135 Taklamakan and Gobi Desert, with a resolution of 45 km, and nested towards Taiwan at a resolution of  
136 15 km (d02) and 5 km (d03) (Fig .1, Table 2). Also, as Taiwan is influenced by biomass burning, the  
137 domain covers up to PSEA, which will be carried out in the future (Ooi et al., 2021). The model consisted  
138 of 40 vertical layers, with eight layers below ~1 KM altitude, 13 layers below ~3 KM altitude, and 27  
139 layers covering the upper layer to ~21 KM. The model's initial and lateral boundary conditions were  
140 constructed using the National Centers for Environmental Prediction (NCEP) Final Analyses (FNL)  
141 reanalysis dataset on a  $0.5^\circ \times 0.5^\circ$  grid. The data assimilation was conducted by grid nudging in all the  
142 domains. The CB06 gas-phase chemical mechanism and the AERO7 aerosol module model were  
143 implemented in CMAQ for the present study.

144 The anthropogenic emission inventories in East Asia, crucial for our research, were obtained from  
145 the MICS-Asia (Model Inter-Comparison Study for Asia) Phase III emission inventory (Li et al., 2017).  
146 The emissions of  $\text{SO}_2$ ,  $\text{NO}_x$ , NMVOC,  $\text{NH}_3$ , CO,  $\text{PM}_{10}$ ,  $\text{PM}_{2.5}$ , BC, OC and  $\text{CO}_2$  has been meticulously  
147 modified, taking into account of the relative changes in China's anthropogenic emissions between 2010  
148 and 2017 (Zheng et al., 2018). Additionally, the modified emission of  $\text{NO}_2$  was adjusted further by the  
149 satellite imagery OMI- $\text{NO}_2$  in January 2023 (Huang et al., 2021). Biogenic emissions for Taiwan were  
150 prepared by the Biogenic Emission Inventory System version 3.09 (BEIS3, Vukovich and Pierce, 2002)  
151 and, for regions outside Taiwan, by the Model of Emissions of Gases and Aerosols from Nature v2.1  
152 (MEGAN, Guenther et al., 2012). TEDS 10.0 (Taiwan Emission Database System, TWEPA, 2011;  
153 <https://erdb.epa.gov.tw/>, last access: 18 January 2024) was used for domain 3 (d03).

154 To ensure the precision of the multiple dry deposition parameterizations, the present research  
155 conducted six simulation scenarios, namely CMAQ\_Off\_PR11, CMAQ\_Dust\_PR11,



156 CMAQ\_Dust\_PR11, CMAQ\_Dust\_E20, CMAQ\_Dust\_S22 and CMAQ\_Dust\_P22. The  
157 CMAQ\_Off\_PR11 scenario did not include the inline dust calculation (Table 3). Meanwhile, the latest  
158 refined integrated dust treatment was implemented in the CMAQ\_Dust\_PR11 scenario (Kong et al.,  
159 2024). Indeed, both CMAQ\_Off\_PR11 and CMAQ\_Dust\_PR11 used the dry deposition mechanism by  
160 Pleim and Ran (2011). The dry deposition mechanism of Emerson et al. (2020), Shu et al. (2022), and  
161 Pleim et al. (2022) were implemented in CMAQ\_Dust\_E20, CMAQ\_Dust\_S22, and CMAQ\_Dust\_P22  
162 scenarios, respectively.

## 163 **2.4 Ancillary dataset**

164 PM<sub>10</sub> (particulate matter  $\leq 10 \mu\text{m}$  in aerodynamic diameter) and PM<sub>2.5</sub> (particulate matter  $\leq 2.5 \mu\text{m}$  in  
165 aerodynamic diameter) concentrations during the dust events in January 2023 were obtained from Lulin  
166 Atmospheric Background Station (LABS; 23.47° N, 120.87° E, 2862 m MSL) and Cape Fuguei (25.30°  
167 N, 121.54° E, 10 m MSL). The Modern Era Retrospective-analysis for Research and Application version  
168 2 (MERRA-2) reanalysis data was used to demonstrate the spatiotemporal distribution of dust without the  
169 influence of clouds. MERRA-2 (Gelaro et al., 2017) is a NASA reanalysis utilizing Goddard Earth  
170 Observing System Data Assimilation System Version 5 (GEOS-5) and covering remotely sensed data at  
171 a native spatial resolution of  $0.5^\circ \times 0.625^\circ$ . Also, Moderate Resolution Imaging Spectroradiometer  
172 (MODIS) Terra satellite images and the level-3 MODIS AOD at 550 nm (MYD08) were obtained from  
173 the U.S. National Aeronautics and Space Administration (<https://worldview.earthdata.nasa.gov/>).

## 174 **3 Results and Discussion**

### 175 **3.1 Observed air quality and weather conditions**

176 Figure 2 shows the dust outbreak over East Asia, displayed by the MODIS Terra sensor and MODIS  
177 AOD at 550 nm from 22-31 January 2023. The satellite image showed the dust claw pattern over East  
178 Asia on 24 and 25 January (Fig. a3, a4). The next day, the same region was covered by a thick cloud, then  
179 another dust plume again widely distributed during 27-30 January 2023. Using MODIS AOD to verify  
180 the dust plume (Han et al., 2012; Kong et al., 2021), the dust plume was distributed in Central China and  
181 northern Taiwan on 24 January 2023. Moreover, the most intense dust plume in the eastern China and



182 East China Sea region was observed on 27 January. Fig. S1 shows the synoptic weather map across the  
183 study domain. On 22-23 January, the southward high-pressure system was responsible for pushing the  
184 pollutant across the Asian Continent, which is consistent with Chuang et al. (2018) and Kong et al. (2021,  
185 2022, 2024) (Fig. S1a-b). The high-pressure system that moved southward will then move eastward  
186 toward the Western Pacific Ocean (Fig S1c-d). Meanwhile, the high-pressure system on the northwest  
187 side again expands in the southeast direction. The second high-pressure system again pushed the pollutant  
188 for the second time and caused the high pollutant problem on 27 January.

189 The impact of East Asian dust on the air quality over the high-altitude western Pacific region was  
190 widely discussed (Kong et al., 2022). Two interesting high pollution events at Mt. Lulin (2862 m above  
191 sea level) during 24-26 Jan and 27-30 January, respectively, are shown in Fig. 3. The latter event was  
192 more intense compared to the earlier one, where the maximum  $PM_{10}$  concentration can reach up to  $35 \mu g$   
193  $m^{-3}$ . Moreover, it was observed that the black carbon concentrations could reach up to a maximum of 400  
194  $ng m^{-3}$ . Based on the *in-situ* measurement, it was interesting to find the mixing state between dust, black  
195 carbon, and brown carbon (Fig. 3c). Different from what has been discussed by Kong et al. (2022), the  
196 long-range transport air pollution at the high-altitude not just merely EAD, but also included the  
197 anthropogenic pollutant from mainland China.

### 198 **3.2 Evaluation of CMAQ dust emission and dry deposition parameterizations**

199 Table 3 shows the statistical analysis of  $PM_{10}$  and  $PM_{2.5}$  concentrations over Cape Fuguei (northern  
200 Taiwan) from 22-31 January under the multiple deposition mechanisms. CMAQ\_Off\_PR11, the  $PM_{10}$   
201 simulation presented without the inline dust calculation, recorded the normalized mean bias (NMB) of  
202 -57.59 %. CMAQ\_Dust\_PR11 improved the simulation over Cape Fuguei (northern Taiwan) by -54.05  
203 % as we included the refined dust treatment (Kong et al., 2024). However, the improvement is  
204 insignificant due to the weak intensity dust episodes and the limitation due to the excessive deposition  
205 mechanism within the model (Kong et al., 2021). Hence, we expanded the sensitivity simulation to  
206 examine the impact of the deposition algorithm on the aerosol prediction. CMAQ\_Dust\_E20 simulations  
207 utilizing the Emerson et al. (2020) approach increased the modeled  $PM_{10}$  simulation by NMB of -41.9 %.





208 In addition, the deposition algorithm proposed by CMAQ\_Dust\_S22 (Shu et al., 2022) and  
209 CMAQ\_Dust\_P22 (Pleim et al., 2020) has reduced the NMB by -47.01 % and -53.90 %, respectively.

210 Instead of PM<sub>10</sub> simulation, the present study found that the inline dust treatment and deposition  
211 algorithms could influence PM<sub>2.5</sub> simulation performances. For instance, the modeled PM<sub>2.5</sub> improved  
212 from -19.55 % (CMAQ\_Off\_PR11) to -16.53 % (CMAQ\_Dust\_PR11). Meanwhile, the deposition  
213 algorithm embedded in CMAQv5.4 has further enhanced the modeled PM<sub>2.5</sub> by -10.65 %, -15.22 %, and  
214 -8.84 % under CMAQ\_Dust\_E20, CMAQ\_Dust\_S22 and CMAQ\_Dust\_P22, respectively. This incident  
215 suggested that the East Asian dust from northwest China transported to the Western Pacific Ocean could  
216 also carry the anthropogenic emission of East China.

217 Figure 4 shows the time series of hourly PM<sub>10</sub> and PM<sub>2.5</sub> concentrations over Cape Fuguei  
218 (northern Taiwan) and Mt. Lulin (high altitude region) from 22-31 January under the multiple deposition  
219 mechanisms. Generally, all the patterns of PM<sub>10</sub> simulations were consistent with the observed PM<sub>10</sub>,  
220 especially in capturing the peak value. For instance, the maximum observed (CMAQ\_Dust\_E20) PM<sub>10</sub>  
221 concentrations at the surface during Jan 24 and Jan 27 were 141 (102.6)  $\mu\text{g m}^{-3}$  and 114 (163.2)  $\mu\text{g m}^{-3}$ ,  
222 respectively. A similar time-series pattern was found for the PM<sub>2.5</sub> simulation (Fig. 4b).

223 The CMAQ model performance over the high-altitude region needed to be carried out and  
224 discussed. The biomass-burning episode of the north peninsula of Southeast Asia over Mt. Lulin has been  
225 finely correlated by plume rise injection (Chuang et al., 2016; Ooi et al., 2021). Meanwhile, the modeled  
226 EAD episodes over Mt. Lulin were due to the convergent pattern over the Asian Continental, which  
227 correlated well with the MERRA2 (Kong et al., 2022). From Fig. 4c, the modeled PM<sub>10</sub> pattern for  
228 CMAQ\_Dust\_Off could not correlate well with observed PM<sub>10</sub> over Mt. Lulin, with a poor correlation of  
229 0.17. The correlation was increased for CMAQ\_Dust\_PR11 (0.47), CMAQ\_Dust\_S22 (0.54),  
230 CMAQ\_Dust\_P22 (0.46), and primarily well performed for CMAQ\_Dust\_E20 (0.55). The modeled result  
231 was somehow consistent with the surface PM<sub>10</sub> simulation at Cape Fuguei. The high observed PM<sub>10</sub>  
232 episodes during 27-28 January with a maximum of 34.5  $\mu\text{g m}^{-3}$  was only 53.3 % higher than



233 CMAQ\_Dust\_E20 of  $22.5 \mu\text{g m}^{-3}$ . For the CMAQ  $\text{PM}_{2.5}$ , the simulation generally underestimated the  
234 observed  $\text{PM}_{2.5}$ .

235 The present work is consistent with the dust scheme in the WRF-Chem, where the dust loading is  
236 very sensitive to the dry deposition schemes and dust emission schemes, especially over the downwind  
237 region (Zeng et al., 2020). Fig. 5 shows the CMAQ estimated ten days averaged mean  $\text{PM}_{10}$  and  $\text{PM}_{2.5}$   
238 for the PR11 deposition scheme and its corresponding change by E20, S22, and P22,  
239 respectively. Generally, the spatial distribution of the high  $\text{PM}_{10}$  concentrations by  $> 80 \mu\text{g m}^{-3}$  was  
240 distributed over northwest China, which is the dust source region's location, consistent with the simulation  
241 suggested by Kong et al. (2021, 2022, 2024). Such high particulate matter dissipated to east China,  
242 indicating the transport pathway in the southeastern direction towards the western Pacific (Fig. 5a). The  
243 difference between E20 and PR11 suggested the high  $\text{PM}_{10} > 50 \mu\text{g m}^{-3}$  distributed over northwest China,  
244 meaning E20 successfully increased the  $\text{PM}_{10}$  concentrations. As compared to the S22 deposition scheme,  
245 it also increased the  $\text{PM}_{10}$  over northwest China by around  $30 \mu\text{g m}^{-3}$  but was not as intense as E20. For  
246 P22, the difference of  $\text{PM}_{10}$  between PR11 and P22 was less than  $10 \mu\text{g m}^{-3}$ , indicating less efficiency of  
247 P22 in improving the  $\text{PM}_{10}$ . Another fascinating fact about E20 was that the  $\text{PM}_{10}$  increased over the  
248 southern South China Sea. For the modeled  $\text{PM}_{2.5}$  concentrations, the high concentration was  
249 distributed over the Asian Continental. Under the E20 mechanism, the modeled  $\text{PM}_{2.5}$  has been  
250 increased over PSEA. For S22, such improvement of  $\text{PM}_{2.5}$  was more intense over a similar region.  
251 Meanwhile, the  $\text{PM}_{2.5}$  simulated by P22 didn't have much difference compared to PR11, which showed  
252 consistency as the  $\text{PM}_{10}$  simulation.

253 During the spring of 2021, a series of dust storms (15 March, 27 March, and 18 April) occurred  
254 over the Gobi area, with one of the most significant dust storms in the past decade (15 March, the "3.15"  
255 dust storm hereafter) causing environmental impact over the continental (Jin et al., 2022; Gui et al., 2022;  
256 He et al., 2022; Liang et al., 2022; Tang et al., 2022). More interestingly, one of the multiple dust storm  
257 episodes reached WPO due to the extreme typhoon episode (Kong et al., 2024). Hence, we intend to re-  
258 emphasize the precision of various deposition schemes on the CMAQ for the recent dust storm episode  
259 highlighted by Kong et al. (2024). As a result, we specially conducted the East Asia region simulation



260 that is d01, for the 3-day averaged sensitivity test for three dust storm episodes: 14-16 March 2021 (“3.15”  
261 dust storm), 26-28 March 2021 (“3.27” dust storm), and 17-19 April 2021 (“4.18” dust storm)  
262 (Table 5). Overall, CMAQ Dust\_E20 above 30°N has evaluated well the MODIS AOD by NMB of -26.2  
263 %, as compared to PR11 (-37.4 %), S22 (-32.0 %) and P22 (-35.8 %). The CMAQ AOD by E20 during  
264 the most intense SDS in 3.15 has significantly improved over northern China, the dust source region, as  
265 shown in the red dash rectangular box (Fig. S2). Additionally, the modeled AOD by E20 over WPO  
266 (shown in red dash rectangular box) increased in episode 4.18, reporting a value of 0.7 compared to 0.4  
267 by PR11. Importantly, the E20 deposition scheme has primarily enhanced the PM<sub>10</sub> prediction over the  
268 marine boundary layer, addressing the model uncertainty due to the typhoon mentioned by Kong et al.  
269 (2024) and demonstrating the practical implications of our research.

### 270 **3.3 Impact on the CMAQ ambient particle concentrations**

271 Figure 6 shows the boxplot of the 10-day averaged simulated  $V_d$  for the Aitken, accumulation, and coarse  
272 particles modes under multiple deposition schemes, namely PR11 (Pleim and Ran, 2011), E20 (Emerson  
273 et al., 2020), S22 (Shu et al., 2022) and P22 (Pleim et al., 2022). The different types of dry deposition  
274 treatments substantially impact aerosol profile, altering the ambient total dry deposition regionally. As  
275 shown in the figure, E20, S22, and P22 increased the deposition velocity of the Aitken (accumulation)  
276 modes particle as compared to PR11 by 22.56 (11.32) %, 117.76 (86.43) % and 2.5 (7.52) % respectively.  
277 The simulation suggested that S22 contained the highest  $V_d$  compared to E20 and P22. For coarse-mode  
278 particles, the P22 simulation median  $V_d$  increased by 14.36 % compared to PR11. On the other hand, E20  
279 and S22 showed a different simulation by the median  $V_d$  reduction by -9.1 % and -12.1 %, respectively.  
280 Also, the 75<sup>th</sup> percentile  $V_d$  has been significantly reduced by -50.57 % and -58.27 %, respectively. The  
281 result suggested that the reduced  $V_d$  of the coarse mode particle was responsible for resolving the PM<sub>10</sub>  
282 simulation underestimation of PR11, consistent with the simulation by Shu et al. (2022) and Ryu and Min  
283 (2022). The slow  $V_d$  means the total loss of aerosol to the surface has been minimized, leading to  
284 increased aerosol concentration.

285 We estimated the CMAQ averaged particle modes for the PR11 dry deposition scheme and the  
286 corresponding percentage changes using E20, S22, and P22 (Fig. 7). By using E20 and S22, we found



287 that the  $V_d$  corresponding to the Aitken and accumulation modes has been increased by >100 % over  
288 most of the CMAQ domain, which was most obvious over Asian continent. Meanwhile, the variation of  
289  $V_d$  distribution was insignificant for P22. For the coarse mode particles, the  $V_d$  has been tremendously  
290 reduced for E20 and S22 compared to PR11. However, for S22, the  $V_d$  has increased by >100 % over  
291 northwest China, which is the dust source region. This leads to a significant deposition over the desert  
292 before transporting it to the downwind region, causing less  $PM_{10}$  simulated by S22 than E20. A previous  
293 study proposed the  $V_d$  for the aerosol at the water surface was associated with the CTM uncertainly at the  
294 downwind region (Kong et al., 2021, 2024; Ryu and Min, 2022). The  $V_d$  of Aitken and accumulation  
295 modes at land and water surfaces increased generally, except E20 at the water surface. Interestingly, the  
296 coarse mode  $V_d$  at the water surface for E20 and S22 decreased significantly by -44.65 % and -21.44 %,  
297 respectively, suggesting that both deposition schemes, particularly E20, could resolve the excessive  
298 deposition over the marine boundary layer, as mentioned by Kong et al. (2021) (Table 6).

### 299 **3.4 CMAQ of dust and black carbon synoptic pattern at the upper level**

300 Black carbon, known as elementary carbon, released from the biofuels, fossil fuels and biomass burning,  
301 has been proven to impact the radiative budget and regional climate (Ramanathan, V and Carmicheal,  
302 2008; Pani et al., 2016, 2020). In the meantime, China has been a significant contributor to global  
303 anthropogenic black carbon emission, particularly in the cities of the northern part (Xiao et al., 2023;  
304 Wang et al., 2024). During the severe dust episodes in the spring of 2023, the contribution of black carbon  
305 brought by EAD was captured in North China (Wang et al., 2024). As depicted in Fig. 2, the  
306 transboundary episode observed in the upper level of Taiwan during this event could be the mixing of the  
307 natural dust and anthropogenic haze episodes, which demonstrates the consistency. Additionally,  
308 blending mineral dust with anthropogenic transport due to the north easterly wind, a wind that blows from  
309 the northeast, has been a subject of extensive discussion (Lin et al., 2007, 2012; Li et al., 2012). During  
310 the EAD, the dust from the Gobi Desert that was transported towards the western Pacific region could  
311 also carry anthropogenic aerosol, contributing to different levels of pollutant concentration. However, the  
312 distinct transport pathway at the high altitude between both aerosol types is a topic that has received less  
313 attention but is of significant importance to our understanding of atmospheric dynamics.



314 Figure 8 illustrates mineral dust concentration's spatial and temporal distribution under the  
315 CMAQ\_Dust\_E20 scenario at 700 hPa from 24-30 January. The model reveals a high proportion of  
316 modeled dust aerosol (red dash circle) at the source region, indicating an uplift from the surface to 700  
317 hPa (Fig. 8a, b). This uplift, driven by the strong pressure gradient at the surface and the 'eastward moving  
318 trough system' at the upper level (700 hPa), is a key factor in the eastward and southward transfer of the  
319 dust (Fig. 8c-d). The high dust fraction reappears at the source region (Fig. 8e, f) and is transported  
320 eastwardly by the similar upper-level trough (Fig. 8g-j), causing a long dust belt at 15°N, distributing  
321 over central Asia continental, Taiwan Straits, Taiwan and large part of western Pacific Ocean. (Fig. 8i, j).  
322 On 29 January, the model of E20 clearly predicted that the dust plume moved in the southward direction  
323 toward the South China Sea (Fig. 8k, l). The dust aerosol was left distributed at a certain part of the  
324 northern South China Sea and the Philippine Sea until it totally dissipated (Fig. 8m, n). This interesting  
325 result suggests the possible EAD at the longer distance at the upper level, which is a topic for further  
326 investigation.

327 The southward high-pressure system responsible for the long-range transport haze episode has  
328 been widely discussed (Chuang et al., 2008; Kong et al., 2021)—however, the upper-level transboundary  
329 transport needs to be addressed more. While focusing on CMAQ\_Dust\_E20, we attempted to characterize  
330 the transboundary of modeled black carbon at the upper level (700 hPa) (Fig. 9). As shown in Fig. 9(c,  
331 e), the modeled black carbon concentration is shown to be significantly distributed at central China. The  
332 black carbon transport pattern followed the eastward-moving trough system as the plume moved eastward  
333 and southward (Fig. 9g-l). Interestingly, the long black carbon belt is consistent with the long dust belt,  
334 as shown in Fig. 8. For instance, both modeled dust and black carbon were distributed at the South China  
335 Sea (Fig. 8m, n; Fig 9m, n). This means that the black carbon due to the anthropogenic emission and the  
336 natural EAD shared a similar transport pattern at the upper level, driven by the trough system. Such  
337 consistency has been verify by the AOD simulated by CMAQ, along with the MERRA-2 dust and black  
338 carbon mass column over the region (Fig .S3).

339 Dust aerosol vertical profiles (Fig. 10) show the large dust fraction was distributed over the Asian  
340 Continent (Fig. 10a, b), according to the transect drawn as a red-dash line in Fig. 1. Due to the westerly



341 winds as illustrated in Fig. 8, the aerosol plume transported at the eastward direction toward the western  
342 Pacific Ocean, that vastly accumulated along the 700 hPa altitude. Another plume was found across the  
343 ocean on the east side of Taiwan Island (Fig. 10b). The plume was moved eastward (Fig. 10c-f). During  
344 00 UTC on 27 January, another large fraction of dust covered the Asian Continent (Fig. 10g); in the next  
345 12 hours, the model showed an apparent dust plume located in the Western Pacific Ocean, with much  
346 higher dust concentrations compared to Fig. 10b. The plume again distributed eastward showed a clear  
347 dust dome (Fig. 10i-j). Then, due to the westerly airflow, the dust aerosol slowly dissipated at the upper  
348 layer of the western Pacific.

349 The vertical profile of the modeled black carbon has a similar transport pattern as mineral dust  
350 (Fig. 11). As shown in Fig. 11h, the modeled black carbon was found distributed at the western Pacific  
351 Ocean. In Fig. 11i, a clear black carbon dome was distributed along 700 hPa, showing a similar pattern  
352 as dust. This simulation proposes the consistency of the “double dome” mechanism of Asian dust and  
353 biomass burning episodes, as the coarse particles could comprise of fine particles (Dong et al., 2018;  
354 Huang and Fu, 2019). The issue regarding whether or not such a mechanism could cause the warming  
355 effect can be considered as a future study. However, the difference is that the dust dome contains a higher  
356 fraction of concentrations as compared to the black carbon dome. Considering the maximum height, the  
357 present simulation suggests the dust aerosol can reach up to 500 hPa, which is consistent with Kong et al.  
358 (2021). Contrary, the black carbon plume was slightly lower with approximately 600 hPa of the maximum  
359 height under the same meteorological condition. As this section essentially discusses the similarity and  
360 distinctiveness of natural dust and anthropogenic aerosol at the upper level, we are interested in  
361 characterizing the synoptic pattern. Hence, the present simulation did not consider the two-way coupling  
362 model, and it is strongly suggested for future study.

#### 363 **4.0 Summary and Conclusions**

364 The chemical transport model is considered sensitive to the dry deposition parameterization besides the  
365 dust emission treatment. The present study demonstrates the impact of the four dry deposition  
366 parameterizations on aerosol performance in East Asia. It provides a significant analysis of the  
367 transboundary transport of East Asian Dust to Taiwan from a case study of 22-31 January 2023. The



368 incorporation of the latest dust emission treatment with PR11 (Pleim and Ran, 2011; Kong et al., 2024)  
369 to the CMAQ slightly improved the model performance to -54.05 % from -57.59 %. While this  
370 improvement may seem insignificant, it underscores our commitment to accuracy in aerosol modeling  
371 and the potential for further advancements in the field. By implementing the E20 dry deposition scheme,  
372 characterized by adding the collection efficiency by interception across the land surface, the CMAQ  
373 simulation of the surface  $PM_{10}$  has been vastly improved by NMB of -41.9 %, as compared to the dry  
374 deposition proposed by S22 (-47.01 %) and P22 (-53.90 %). Moreover, the modeled  $PM_{10}$  pattern by  
375 CMAQ\_Dust\_E20 at the upper level (700 hPa) was mostly consistent with the observed  $PM_{10}$ , especially  
376 in capturing the peak value. The dry deposition of E20 was correlated well with the high altitude in-situ  
377 by 0.55, as compared to PR11 (0.47), S22 (0.54) and P22 (0.46). Such a significant difference in  $PM_{10}$   
378 improvement has also been shown by modeled  $PM_{2.5}$ . The simulation of surface  $PM_{2.5}$  by PR11 has been  
379 improved to -16.53 % from -19.55 %, after using the latest dust treatment, and further enhanced by E20  
380 (-10.65 %), S22 (-15.22 %) and P22 (-8.84 %). Additionally, the CMAQ\_Dust\_E20 treatment provided  
381 an optimized AOD simulation value for the multiple dust storm episodes in spring 2021.

382 The previous CMAQ model, modulated by Kong et al. (2021; 2024), showed excessive deposition  
383 at the marine boundary layer, leading to an underestimation of the modeled surface  $PM_{10}$ . However, our  
384 updated model, using the E20 and S22 schemes over the entire model domain, has not just reduced, but  
385 significantly reduced the 75<sup>th</sup> percentile of  $V_d$  by -50.57 % and -58.27 %, respectively. This precise  
386 reduction of  $V_d$  of the coarse mode particle, responsible for resolving the  $PM_{10}$  simulation  
387 underestimation, has not just minimized, but effectively minimized the total loss of aerosol to the surface,  
388 leading to a concentration increment. Furthermore, the intense decrease of modeled  $V_d$  across the water  
389 surface by E20 could play a crucial role in resolving the excessive aerosol deposition over the ocean  
390 layer. These precise adjustments in the model's parameters demonstrate our commitment to improving  
391 the accuracy of aerosol modeling and should inspire confidence in the results of our research.

392 In addition, the updated CMAQ was used to investigate the synoptic pattern at the upper  
393 level. The transboundary transport of EAD from the Asian Continent towards the western Pacific Ocean  
394 at the upper level was associated with the eastward moving trough system. Such transport mechanism is



395 found to bring along the black carbon aerosol, which is primarily the main element of China's human-  
396 made emissions. More interestingly, both aerosol profiles created a "long dust-black carbon belt" along  
397 the 15°N. The 'double dome mechanism', a concept proposed by Huang et al. (2019) that depicts the  
398 superposition of the two types of aerosol, was also simulated in the present study. However, since the  
399 present work did not consider two-way radiative impact, the issue of warming/cooling is proposed in the  
400 future study.

#### 401 **Data Availability**

402 MERRA-2 data are available online through the NASA Goddard Earth Sciences Data Information  
403 Services Center (GES DISC; <https://disc.gsfc.nasa.gov>; last access: 01 August 2024). MODIS data used  
404 in this study are available at <https://asdc.larc.nasa.gov/>(last access: 01 August 2024). The observational  
405 data at LABS can be ordered by contacting corresponding authors.

#### 406 **Author Contribution**

407 **Steven Soon-Kai Kong:** Conceptualization; Data curation; Formal analysis; Investigation; Methodology;  
408 Software; Validation; Visualization; Writing – original draft; Writing – review and editing.

409 **Joshua S. Fu:** Conceptualization; Investigation; Methodology; Formal analysis; Writing – review and  
410 editing.

411 **Neng-Huei Lin:** Conceptualization; Visualization; Supervision; Funding acquisition; Resources; Writing  
412 – review and editing.

413 **Guey-Rong Sheu:** Funding acquisition; Resources.

414 **Wei-Syun Huang:** Data curation; Software.

#### 415 **Competing Interests**

416 Some authors are members of the editorial board of journal ACP.





## 417 **Acknowledgments**

418 We acknowledged the National Science and Technology Council of Taiwan, under Project No.  
419 NSTC113-2811-M-008-045 for supporting the research. We also acknowledged the staff at LABS, and  
420 EPA Taiwan for the provision of the ground-based measurement datasets. We are also thankful to  
421 MERRA-2 and MODIS for the satellite product.

## 422 **References:**

- 423 Chuang, M., Fu, J. S., Lee, C., Lin, N., Gao, Y., Wang, S., Sheu, G., Hsiao, T., Wang, J., Yen, M., Lin,  
424 T., and Thongboonchoo, N.: The Simulation of Long-Range Transport of Biomass Burning Plume and  
425 Short-Range Transport of Anthropogenic Pollutants to a Mountain Observatory in East Asia during the  
426 7-SEAS / 2010 Dongsha Experiment, 2933–2949, <https://doi.org/10.4209/aaqr.2015.07.0440>, 2016.
- 427 Chuang, M. T., Fu, J. S., Jang, C. J., Chan, C. C., Ni, P. C., and Lee, C. Te: Simulation of long-range  
428 transport aerosols from the Asian Continent to Taiwan by a Southward Asian high-pressure system, *Sci.*  
429 *Total Environ.*, 406, 168–179, <https://doi.org/10.1016/j.scitotenv.2008.07.003>, 2008.
- 430 Dong, X., Fu, J. S., Huang, K., Tong, D., and Zhuang, G.: Model development of dust emission and  
431 heterogeneous chemistry within the Community Multiscale Air Quality modeling system and its  
432 application over East Asia, 8157–8180, <https://doi.org/10.5194/acp-16-8157-2016>, 2016.
- 433 Dong, X., Fu, J. S., Huang, K., Lin, N., Wang, S., and Yang, C.: Analysis of the Co-existence of Long-  
434 range Transport Biomass Burning and Dust in the Subtropical West Pacific Region, *Sci. Rep.*, 1–10,  
435 <https://doi.org/10.1038/s41598-018-27129-2>, 2018.
- 436 Emerson, E. W., Hodshire, A. L., DeBolt, H. M., Bilsback, K. R., Pierce, J. R., McMeeking, G. R., and  
437 Farmer, D. K.: Revisiting particle dry deposition and its role in radiative effect estimates, *Proc. Natl.*  
438 *Acad. Sci. U. S. A.*, 117, 26076–26082, <https://doi.org/10.1073/pnas.2014761117>, 2020.
- 439 Foroutan, H., Young, J., Napelenok, S., Ran, L., Appel, K., Gilliam, R., and Pleim, J.: *Journal of Advances*  
440 *in Modeling Earth Systems*, *J. Adv. Model. Earth Syst.*, 9, 585–606,  
441 <https://doi.org/10.1002/2013MS000282>.Received, 2017.
- 442 Gaydos, T. M., Pinder, R., Koo, B., Fahey, K. M., Yarwood, G., and Pandis, S. N.: Development and  
443 application of a three-dimensional aerosol chemical transport model, *PMCAMx*, *Atmos. Environ.*, 41,



- 444 2594–2611, <https://doi.org/10.1016/j.atmosenv.2006.11.034>, 2007.
- 445 Gelaro, R., McCarty, W., Suárez, M. J., Todling, R., Molod, A., Takacs, L., Randles, C. A., Darmenov,  
446 A., Bosilovich, M. G., Reichle, R., Wargan, K., Coy, L., Cullather, R., Draper, C., Akella, S., Buchard,  
447 V., Conaty, A., da Silva, A. M., Gu, W., Kim, G. K., Koster, R., Lucchesi, R., Merkova, D., Nielsen, J.  
448 E., Partyka, G., Pawson, S., Putman, W., Rienecker, M., Schubert, S. D., Sienkiewicz, M., and Zhao, B.:  
449 The modern-era retrospective analysis for research and applications, version 2 (MERRA-2), *J. Clim.*, 30,  
450 5419–5454, <https://doi.org/10.1175/JCLI-D-16-0758.1>, 2017.
- 451 Giardina, M. and Buffa, P.: A new approach for modeling dry deposition velocity of particles, *Atmos.*  
452 *Environ.*, 180, 11–22, <https://doi.org/10.1016/j.atmosenv.2018.02.038>, 2018.
- 453 Gui, K., Yao, W., Che, H., An, L., Zheng, Y., Li, L., Zhao, H., Zhang, L., Zhong, J., Wang, Y., and Zhang,  
454 X.: Record-breaking dust loading during two mega dust storm events over northern China in March 2021:  
455 aerosol optical and radiative properties and meteorological drivers, *Atmos. Chem. Phys.*, 22, 7905–7932,  
456 <https://doi.org/10.5194/acp-22-7905-2022>, 2022.
- 457 Han, X., Ge, C., Tao, J., Zhang, M., and Zhang, R.: Air quality modeling for a strong dust event in East  
458 Asia in March 2010, *Aerosol Air Qual. Res.*, 12, 615–628, <https://doi.org/10.4209/aaqr.2011.11.0191>,  
459 2012.
- 460 He, Y., Yi, F., Yin, Z., Liu, F., Yi, Y., and Zhou, J.: Mega Asian dust event over China on 27–31 March  
461 2021 observed with space-borne instruments and ground-based polarization lidar, *Atmos. Environ.*, 285,  
462 119238, <https://doi.org/10.1016/j.atmosenv.2022.119238>, 2022.
- 463 Huang, K., Fu, J. S., Lin, N.-H., Wang, S.-H., Dong, X., & Wang, G.: Superposition of Gobi dust and  
464 Southeast Asian biomass burning: The effect of multisource long-range transport on aerosol optical  
465 properties and regional meteorology modification. *J. Geophys. Res. Atmos.*, 124, 9464–9483,  
466 <https://doi.org/10.1029/2018JD030241>, 2019.
- 467 Huang, W. S., Griffith, S. M., Lin, Y. C., Chen, Y. C., Lee, C. Te, Chou, C. C. K., Chuang, M. T., Wang,  
468 S. H., and Lin, N. H.: Satellite-based emission inventory adjustments improve simulations of long-range  
469 transport events, *Aerosol Air Qual. Res.*, 21, 1–16, <https://doi.org/10.4209/AAQR.210121>, 2021.
- 470 Jin, J., Pang, M., Segers, A., Han, W., Fang, L., Li, B., Feng, H., Lin, H. X., and Liao, H.: Inverse  
471 modeling of the 2021 spring super dust storms in East Asia, *Atmos. Chem. Phys.*, 22, 6393–6410,



- 472 <https://doi.org/10.5194/acp-22-6393-2022>, 2022.
- 473 Khan, T. R. and Perlinger, J. A.: Evaluation of five dry particle deposition parameterizations for  
474 incorporation into atmospheric transport models, *Geosci. Model Dev.*, 10, 3861–3888,  
475 <https://doi.org/10.5194/gmd-10-3861-2017>, 2017.
- 476 Kok, J. F., Parteli, E. J. R., Michaels, T. I., Karam, D. B., and Pierre, U.: The physics of wind-blown sand  
477 and dust, 1–119, n.d.
- 478 Kong, S. S., Fu, J. S., Dong, X., Chuang, M., Chel, M., Ooi, G., Huang, W., Griffith, S. M., Kumar, S.,  
479 and Lin, N.: Sensitivity analysis of the dust emission treatment in CMAQv5 . 2 . 1 and its application to  
480 long-range transport over East Asia, *Atmos. Environ.*, 118441,  
481 <https://doi.org/10.1016/j.atmosenv.2021.118441>, 2021.
- 482 Kong, S. S. K., Pani, S. K., Griffith, S. M., Ou-Yang, C. F., Babu, S. R., Chuang, M. T., Ooi, M. C. G.,  
483 Huang, W. S., Sheu, G. R., and Lin, N. H.: Distinct transport mechanisms of East Asian dust and the  
484 impact on downwind marine and atmospheric environments, *Sci. Total Environ.*, 827,  
485 <https://doi.org/10.1016/j.scitotenv.2022.154255>, 2022.
- 486 Kong, S. S. K., Ravindra Babu, S., Wang, S. H., Griffith, S. M., Chang, J. H. W., Chuang, M. T., Sheu,  
487 G. R., and Lin, N. H.: Expanding the simulation of East Asian super dust storms: physical transport  
488 mechanisms impacting the western Pacific, *Atmos. Chem. Phys.*, 24, 1041–1058,  
489 <https://doi.org/10.5194/acp-24-1041-2024>, 2024.
- 490 Li, M., Zhang, Q., Kurokawa, J., Woo, J., He, K., Lu, Z., and Ohara, T.: MIX : a mosaic Asian  
491 anthropogenic emission inventory under the international collaboration framework of the MICS-Asia and  
492 HTAP, 935–963, <https://doi.org/10.5194/acp-17-935-2017>, 2017.
- 493 Liang, L., Han, Z., Li, J., Xia, X., Sun, Y., Liao, H., Liu, R., and Liang, M.: Science of the Total  
494 Environment Emission , transport , deposition , chemical and radiative impacts of mineral dust during  
495 severe dust storm periods in March 2021 over East Asia, *Sci. Total Environ.*, 852, 158459,  
496 <https://doi.org/10.1016/j.scitotenv.2022.158459>, 2022.
- 497 Liu, S., Xing, J., Sahu, S. K., Liu, X., Liu, S., Jiang, Y., Zhang, H., Li, S., Ding, D., Chang, X., and Wang,  
498 S.: Wind-blown dust and its impacts on particulate matter pollution in Northern China: Current and future  
499 scenarios, *Environ. Res. Lett.*, 16, 114041, <https://doi.org/10.1088/1748-9326/ac31ec>, 2021.



- 500 Massad, R. S., Nemitz, E., and Sutton, M. A.: Review and parameterisation of bi-directional ammonia  
501 exchange between vegetation and the atmosphere, *Atmos. Chem. Phys.*, 10, 10359–10386,  
502 <https://doi.org/10.5194/acp-10-10359-2010>, 2010.
- 503 Nemitz, E., Milford, C., and Sutton, M. A.: A two-layer canopy compensation point model for describing  
504 bi-directional biosphere-atmosphere exchange of ammonia, *Q. J. R. Meteorol. Soc.*, 127, 815–833,  
505 <https://doi.org/10.1256/smsqj.57305>, 2001.
- 506 Ooi, M., Chuang, M.-T., Fu, J., Kong, S., Huang, W.-S., Wang, S.-H., Chan, A., Pani, S., and Lin, N.-H.:  
507 Improving prediction of trans-boundary biomass burning plume dispersion: from northern peninsular  
508 Southeast Asia to downwind western north Pacific Ocean, *Atmos. Chem. Phys.*, 1–36,  
509 <https://doi.org/10.5194/acp-2020-1283>, 2021.
- 510 Pani, S. K., Wang, S. H., Lin, N. H., Lee, C. Te, Tsay, S. C., Holben, B. N., Janjai, S., Hsiao, T. C.,  
511 Chuang, M. T., and Chantara, S.: Radiative effect of springtime biomass-burning aerosols over northern  
512 indochina during 7-SEAS/BASELInE 2013 campaign, *Aerosol Air Qual. Res.*, 16, 2802–2817,  
513 <https://doi.org/10.4209/aaqr.2016.03.0130>, 2016.
- 514 Pani, S. K., Wang, S. H., Lin, N. H., Chantara, S., Lee, C. Te, and Thepnuan, D.: Black carbon over an  
515 urban atmosphere in northern peninsular Southeast Asia: Characteristics, source apportionment, and  
516 associated health risks, *Environ. Pollut.*, 259, 113871, <https://doi.org/10.1016/j.envpol.2019.113871>,  
517 2020.
- 518 Pleim, J. and Ran, L.: Surface flux modeling for air quality applications, *Atmosphere (Basel)*, 2, 271–  
519 302, <https://doi.org/10.3390/atmos2030271>, 2011.
- 520 Pleim, J. E., Ran, L., Saylor, R. D., Willison, J., and Binkowski, F. S.: A New Aerosol Dry Deposition  
521 Model for Air Quality and Climate Modeling, *J. Adv. Model. Earth Syst.*, 14, 1–21,  
522 <https://doi.org/10.1029/2022MS003050>, 2022.
- 523 Ramanathan, V and Carmichael, G.: Climate change due to BC, *Nat. Geosci.*, 1, 221–227, 2008.
- 524 Ryu, Y. H. and Min, S. K.: Improving Wet and Dry Deposition of Aerosols in WRF-Chem: Updates to  
525 Below-Cloud Scavenging and Coarse-Particle Dry Deposition, *J. Adv. Model. Earth Syst.*, 14,  
526 <https://doi.org/10.1029/2021MS002792>, 2022.
- 527 Saylor, R. D., Baker, B. D., Lee, P., Tong, D., Pan, L., and Hicks, B. B.: The particle dry deposition



528 component of total deposition from air quality models: right, wrong or uncertain?, *Tellus, Ser. B Chem.*  
529 *Phys. Meteorol.*, 71, 1–22, <https://doi.org/10.1080/16000889.2018.1550324>, 2019.

530 Shu, Q., Koo, B., Yarwood, G., and Henderson, B. H.: Strong influence of deposition and vertical mixing  
531 on secondary organic aerosol concentrations in CMAQ and CAMx, *Atmos. Environ.*, 171, 317–329,  
532 <https://doi.org/10.1016/j.atmosenv.2017.10.035>, 2017.

533 Shu, Q., Murphy, B., Schwede, D., Henderson, B. H., Pye, H. O. T., Appel, K. W., Khan, T. R., and  
534 Perlinger, J. A.: Improving the particle dry deposition scheme in the CMAQ photochemical modeling  
535 system, *Atmos. Environ.*, 289, 119343, <https://doi.org/10.1016/j.atmosenv.2022.119343>, 2022.

536 Slinn, W. G. N.: Predictions for particle deposition to vegetative canopies, *Atmos. Environ.*, 16, 1785–  
537 1794, [https://doi.org/10.1016/0004-6981\(82\)90271-2](https://doi.org/10.1016/0004-6981(82)90271-2), 1982.

538 Tang, W., Dai, T., Cheng, Y., Wang, S., and Liu, Y.: A Study of a Severe Spring Dust Event in 2021 over  
539 East Asia with WRF-Chem and Multiple Platforms of Observations, *Remote Sens.*, 14, 3795,  
540 <https://doi.org/10.3390/rs14153795>, 2022.

541 Wang, W., Zhou, H., Lyu, R., Shao, L., Li, W., Xing, J., Zhao, Z., Li, X., Zhou, X., and Zhang, D.:  
542 Organic Carbon and Elemental Carbon in Two Dust Plumes at a Coastal City in North China, *Aerosol*  
543 *Air Qual. Res.*, 24, <https://doi.org/10.4209/aaqr.240002>, 2024.

544 Wesley, M. L.: Parameterization of Surface Resistances to Gaseous Dry Deposition in Regional-Scale  
545 Numerical Models, *Atmos. Environ.*, 23, 1293–1304, 1989.

546 Xiao, H. W., Xu, Y., and Xiao, H. Y.: Source apportionment of black carbon aerosols in winter across  
547 China, *Atmos. Environ.*, 298, <https://doi.org/10.1016/j.atmosenv.2023.119622>, 2023.

548 Zeng, Y., Wang, M., Zhao, C., Chen, S., Liu, Z., Huang, X., and Gao, Y.: WRF-Chem v3.9 simulations  
549 of the East Asian dust storm in May 2017: Modeling sensitivities to dust emission and dry deposition  
550 schemes, *Geosci. Model Dev.*, 13, 2125–2147, <https://doi.org/10.5194/gmd-13-2125-2020>, 2020.

551 Zhang, L., Gong, S., Padro, J., and Barrie, L.: A size-segregated particle dry deposition scheme for an  
552 atmospheric aerosol module, *Atmos. Environ.*, 35, 549–560, [https://doi.org/10.1016/S1352-](https://doi.org/10.1016/S1352-2310(00)00326-5)  
553 [2310\(00\)00326-5](https://doi.org/10.1016/S1352-2310(00)00326-5), 2001.

554 Zheng, B., Tong, D., Li, M., Liu, F., Hong, C., Geng, G., Li, H., Li, X., and Peng, L.: Trends in China ' s  
555 anthropogenic emissions since 2010 as the consequence of clean air actions, *Atmos. Chem. Phys.*, 18,



556 14095–14111, <https://doi.org/10.5194/acp-18-14095-2018>, 2018.

557

558

559

560

561

562

563

564

565

566

567

568

569

570

571

572

573

574

575

576

577

578

579

580

581

582

583



584 **Table 1.** Detailed mechanism expression relating dry deposition velocity and resistance parameters.

Mechanisms	$V_d$	$R_a$	$R_b$	$R_s$
Pleim and Ran (2011)	$\frac{1}{R_a + R_b + R_s}$	$\frac{\ln\left(\frac{ZR}{ZO}\right) - \psi H}{\kappa u_*}$	$\frac{B^{-1} \left(\frac{Sc}{Pr}\right)^{2/3}}{u_*}$	$\left(\frac{1}{R_{st}} + \frac{1}{R_w} + \frac{1}{R_g}\right)^{-1}$
Emerson et al. (2020)	$V_g + \frac{1}{R_a + R_s}$	$\frac{\ln\left(\frac{ZR}{ZO}\right) - \psi H}{\kappa u_*}$	0	$\frac{1}{\mathcal{E}_0 u_* (E_b + E_{im} + E_{in}) R}$
Pleim et al. (2022)	$\frac{V_g}{1 - \exp(-V_g(R_a + R_b))}$	$\frac{\ln\left(\frac{ZR}{ZO}\right) - \psi H}{\kappa u_*}$	$\frac{V_g}{LAI \cdot u_* (E_B + E_{im} + E_{in}) R}$	0
Shu et al. (2022)	$\frac{V_g}{1 - \exp(-V_g(R_a + R_s))}$	$\frac{\ln\left(\frac{ZR}{ZO}\right) - \psi H}{\kappa u_*}$	0	$\frac{1}{(1 + f_{veg}(\max(LAI - 1, 0)) F_f u_* (E_b + E_{im}))}$

- 585  $V_d$  = deposition velocity  
 586  $V_g$  = settling velocity  
 587  $R_a$  = aerodynamic resistance  
 588  $R_b$  = quasi-laminar boundary layer  
 589  $R_s$  = surface resistance  
 590  $R_{st}$  = stomatal resistance  
 591  $R_w$  = cuticular resistance  
 592  $R_g$  = ground resistance  
 593  $B^{-1}$  = inverse Stanton number  
 594  $u_*$  = frictional velocity  
 595  $Sc$  = Schmidt number  
 596  $Pr$  = analogous quantity for heat  
 597  $LAI$  = Leaf area index  
 598  $E_B$  = Brownian collection efficiency  
 599  $E_{im}$  = Impaction efficiency  
 600  $E_{in}$  = Interception efficiency  
 601  $R$  = rebound factor  
 602  $\mathcal{E}_0$  = deposition velocity  
 603  $f_{veg}$  = grid cell vegetation coverage

604  
 605  
 606  
 607  
 608  
 609  
 610  
 611  
 612  
 613  
 614  
 615  
 616



617 **Table 2.** Model settings.

Model setting	Descriptions
Period	14-16 March 2021, 26-28 March 2021, 17-19 April 2021 and 22-31 January 2023
Domain	d01, d02 and d03 with 45 KM, 15 KM and 5 KM of the resolutions, respectively
Boundary condition	NCEP FNL lateral boundary condition
Surface and land surface model	NOAH
Numerical weather model	WRF v40, including grid and observation nudging at d01.
Chemical transport model	CMAQ v5.4
Gas-phase chemistry and aerosol mechanism	CB06e51 + AE7
Emission Inventory	MICS-ASIA III emission on 2023, adjusted from the emission 2017 (Zhang et al., 2018) based on OMI-NO <sub>x</sub> satellite (Huang et al., 2021).
Online dust treatment	The windblown dust treatment suggested by Kong et al. (2024).

618

619 **Table 3.** Simulation scenarios used in this present study.

Scenarios	Descriptions
CMAQ_Off_PR11	Without in-line calculation of dust, with the dry deposition algorithm by Pleim and Ran (2011).
CMAQ_Dust_PR11	Implement the latest refined dust treatment proposed by Kong et al. (2024), with the dry deposition algorithm by Pleim and Ran (2011).
CMAQ_Dust_E20	Same as CMAQ_Dust_PR11, but with the dry deposition algorithm by Emerson et al. (2020).
CMAQ_Dust_S22	Same as CMAQ_Dust_PR11, but with the dry deposition algorithm by Shu et al. (2022).
CMAQ_Dust_P22	Same as CMAQ_Dust_PR11, but with the dry deposition algorithm by Pleim et al. (2022).

620

621

622

623

624

625

626

627

628

629

630

631

632





633 **Table 4.** Statistical evaluation for PM<sub>10</sub> and PM<sub>2.5</sub> concentrations during 22-31 January 2023 for Cape  
 634 Fuguei under the multiple simulation scenarios.

	Benchmark	CMAQ			CMAQ	
		Off_PR11	Dust_PR11	Dust_E20	Dust_S22	Dust_P22
<b>PM<sub>10</sub></b>						
MeanObs		49.97	49.97	49.97	49.97	49.97
MeanMod		21.19	22.97	29.04	23.04	26.48
NMSE		0.82	0.71	0.49	0.71	0.56
NMB	± 85%	-57.59	-54.05	-41.90	-53.90	-47.01
Corr	> 0.35	0.41	0.44	0.52	0.42	0.46
NMBF		-1.36	-1.18	-0.72	-1.17	-0.89
<b>PM<sub>2.5</sub></b>						
MeanObs		15.52	15.52	15.52	15.52	15.52
MeanMod		12.48	12.95	13.86	13.16	14.15
NMSE		0.31	0.29	0.29	0.31	0.30
NMB	± 85%	-19.55	-16.53	-10.65	-15.22	-8.84
Corr	> 0.35	0.52	0.55	0.53	0.52	0.53
NMBF		-0.24	-0.20	-0.12	-0.18	-0.10

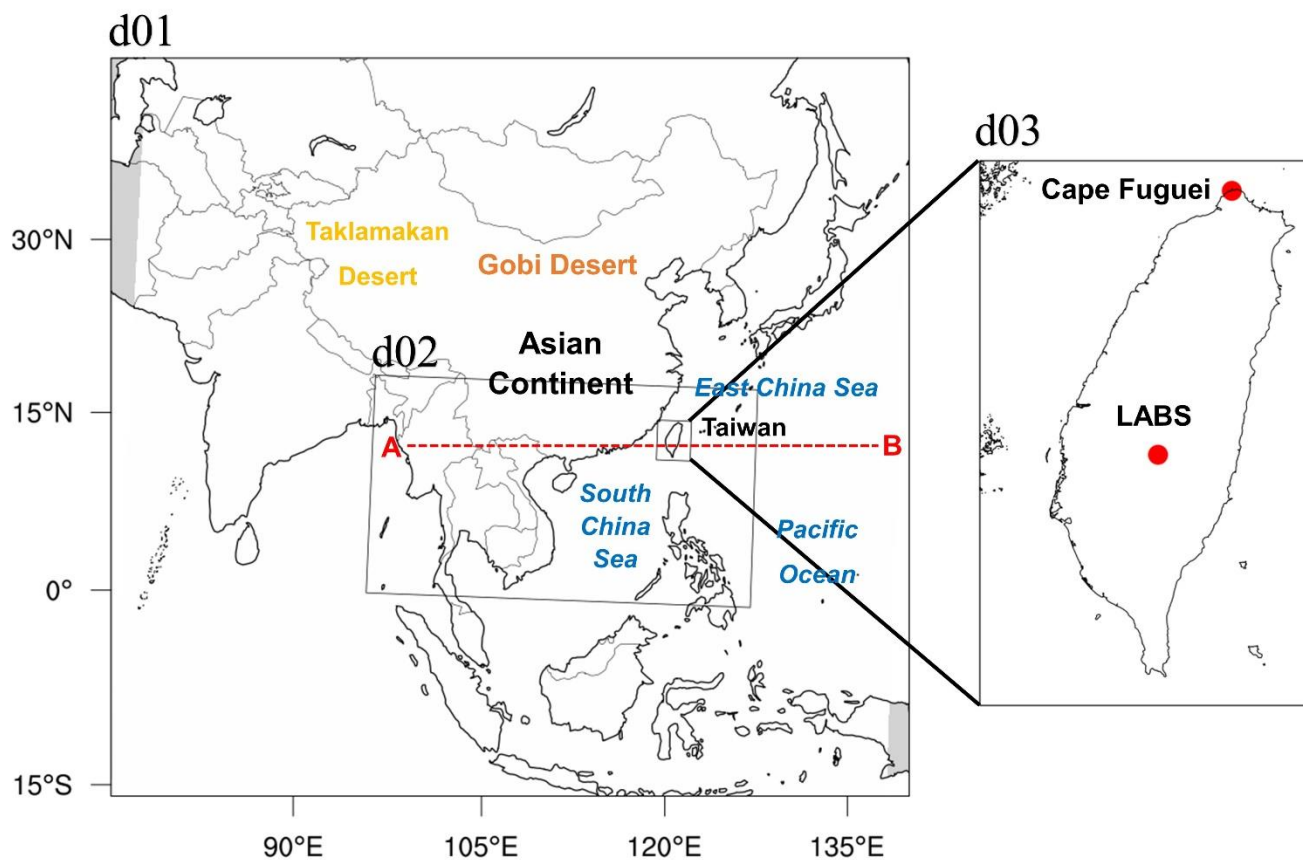
635  
 636 **Table 5.** CMAQ AOD evaluation against MODIS daily observation nearby the dust source region (above  
 637 30°N) with Normalized Mean Bias (NMB) for the multiple simulation scenarios during the dust storm  
 638 episode of 3.15 (14-16 March 2021), 3.27 (26-28 March 2021) and 4.18 (17-19 April 2021).

Cases	3.15	3.27	4.18	Mean
CMAQ_Off_PR11	-81.92	-75.10	-55.88	-70.97
CMAQ_Dust_PR11	-49.54	-46.12	-16.49	-37.38
CMAQ_Dust_E20	-38.97	-36.39	-3.20	-26.19
CMAQ_Dust_S22	-46.41	-41.84	-7.83	-32.03
CMAQ_Dust_P22	-48.45	-44.52	-14.52	-35.83

639  
 640 **Table 6.** Percentage change by PR11 corresponding to E20, S22 and P22, for Aitken, accumulation and  
 641 coarse modes over land and ocean boundary layer.

Changes (%)	Aitken		Accumulation		Coarse	
	Land	Ocean	Land	Ocean	Land	Ocean
E20	12.66	20.06	5.43	-5.19	-47.10	-44.65
S22	173.74	89.45	96.52	52.35	-70.29	-21.44
P22	6.10	1.37	17.66	1.52	10.06	6.86

642  
 643  
 644



645

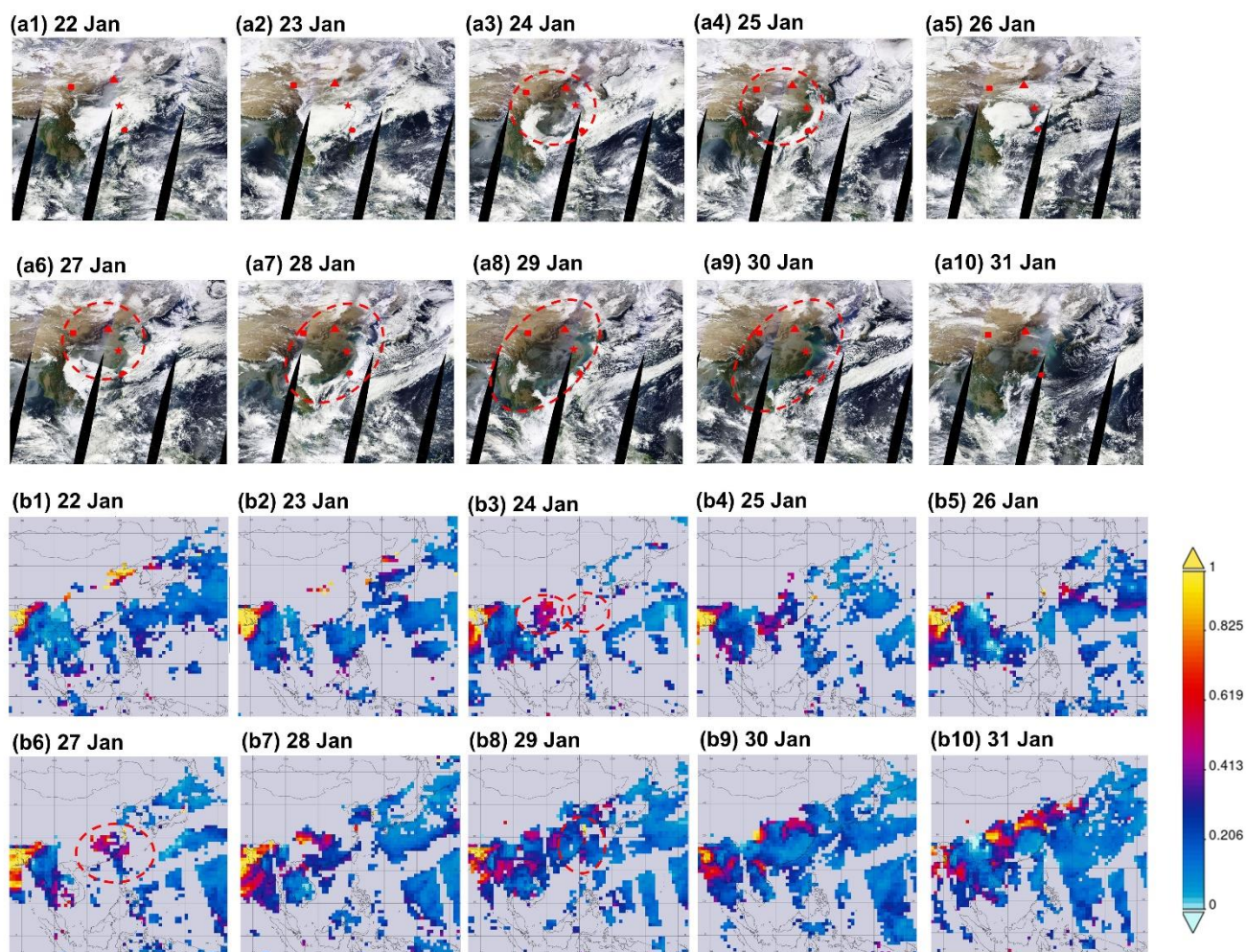
646 **Figure 1:** Modeling domain configuration in East Asia. Ground-based air quality stations in Taiwan at  
647 Cape Fuguei and Lulin Atmospheric Background Station (LABS) are shown in the zoomed panel. The  
648 red dash line (A→B) represents the transects that the aerosol plumes traveled along in this study and that  
649 are discussed in Section 3.4;

650

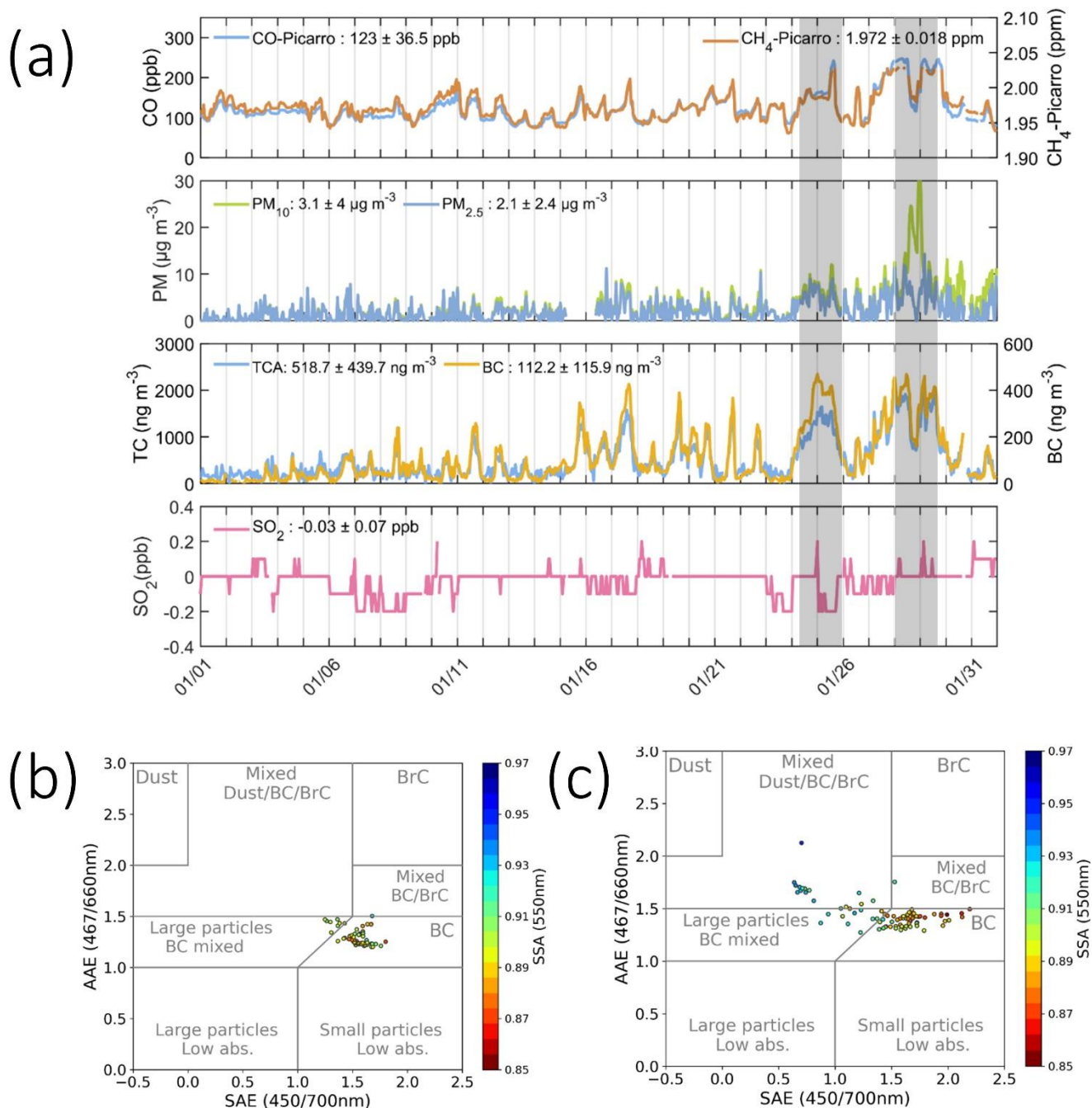
651

652

653



654  
655 **Figure 2:** MODIS Terra images (a1-a10) and MODIS aerosol optical depth AOD at 550 nm (b1-b10)  
656 showing dust outbreak across East Asia during 22-31 January 2023. Red Rectangular, triangle, star and  
657 circle indicate Lanzhou, Beijing, Shanghai and Taiwan. The red circle with dash line indicates the dust  
658 plume.  
659



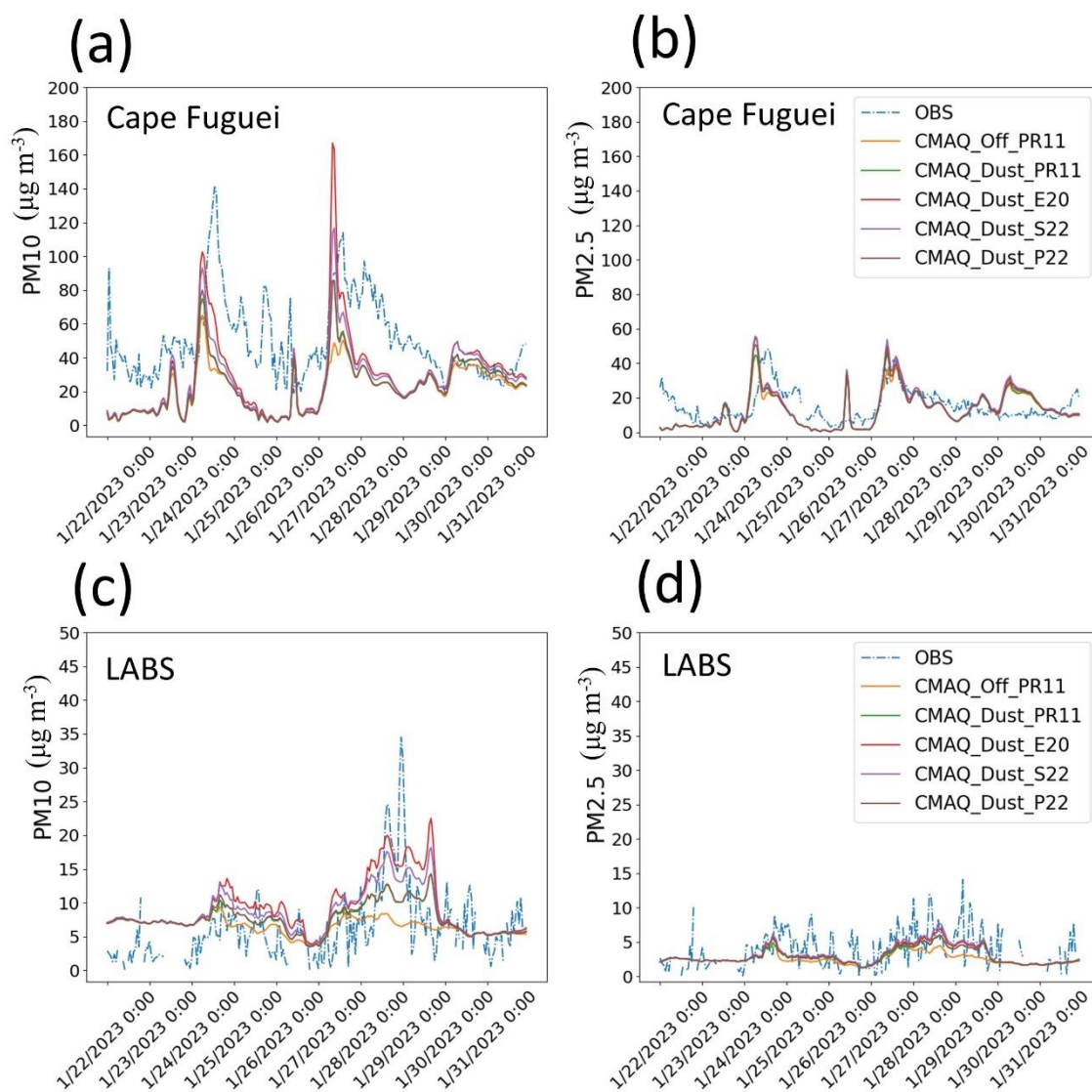
660

661 **Figure 3:** (a) Time series of observed pollutants over LABS during January 2023. The aerosol radiation

662 properties during (b) 24-26 January and (c) 27-30 January 2023.

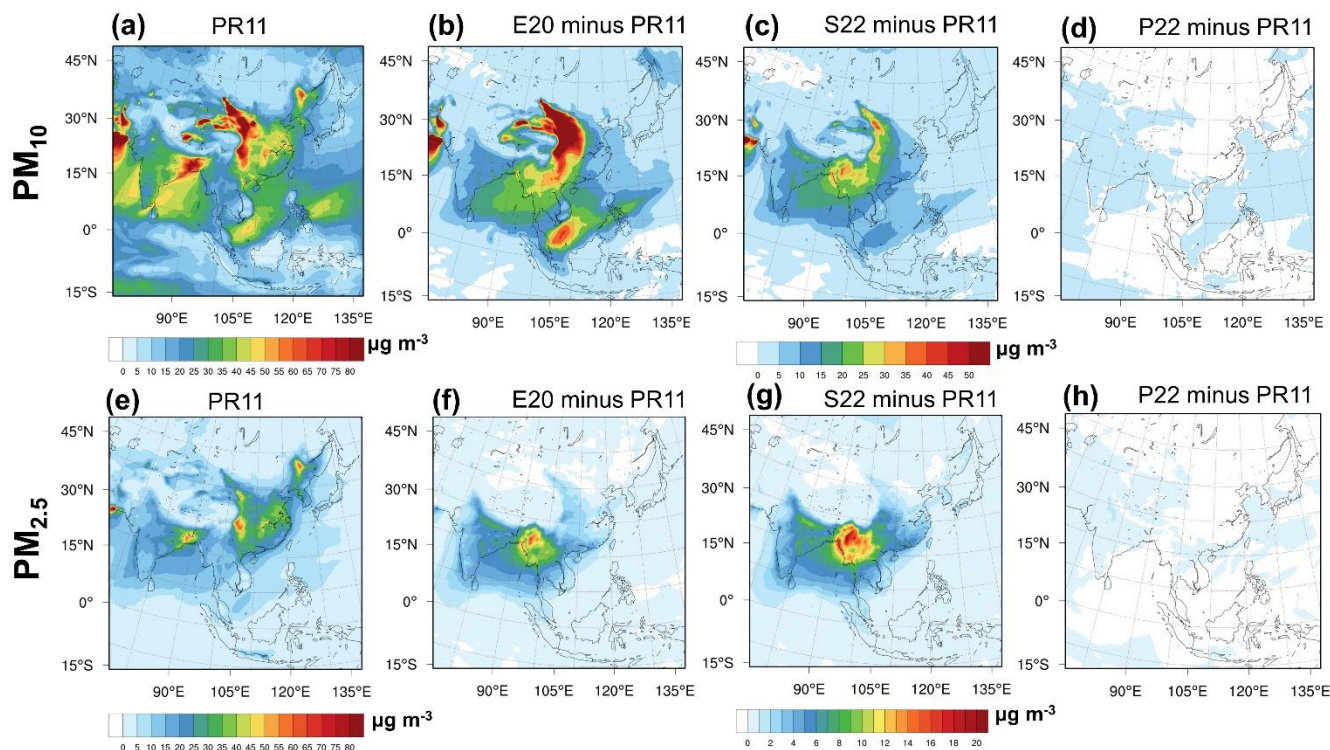


663



664

665 **Figure 4:** Time series of PM<sub>10</sub> (left panel) and PM<sub>2.5</sub> (right panel) concentrations under multiple  
666 deposition schemes over the Cape Fuguei (upper panel) and LABS (lower panel), representing the  
667 surface and high altitude, respectively.



668

669 **Figure 5:** CMAQ estimated 10 days (22-31 January 2023) averaged mean (a-d)  $PM_{10}$  and (e-h)  $PM_{2.5}$  for  
670 (a, e) PR11 dry deposition scheme and the corresponding concentration changes using (b, f) E20, (c, g)  
671 S22 and (d, h) P22 schemes.

672

673

674

675

676

677

678

679

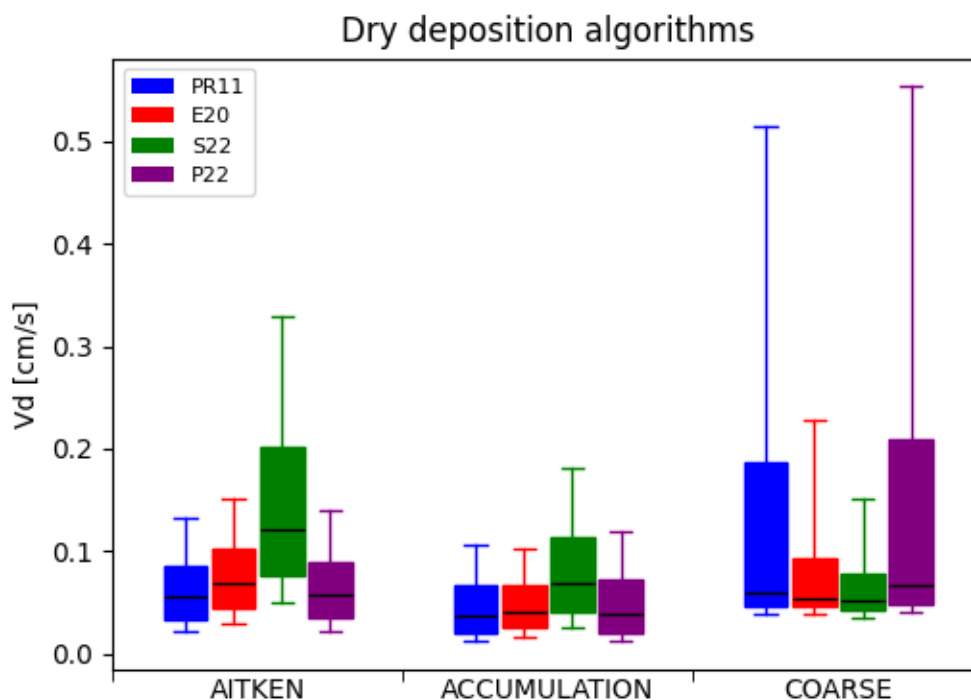
680

681

682



683

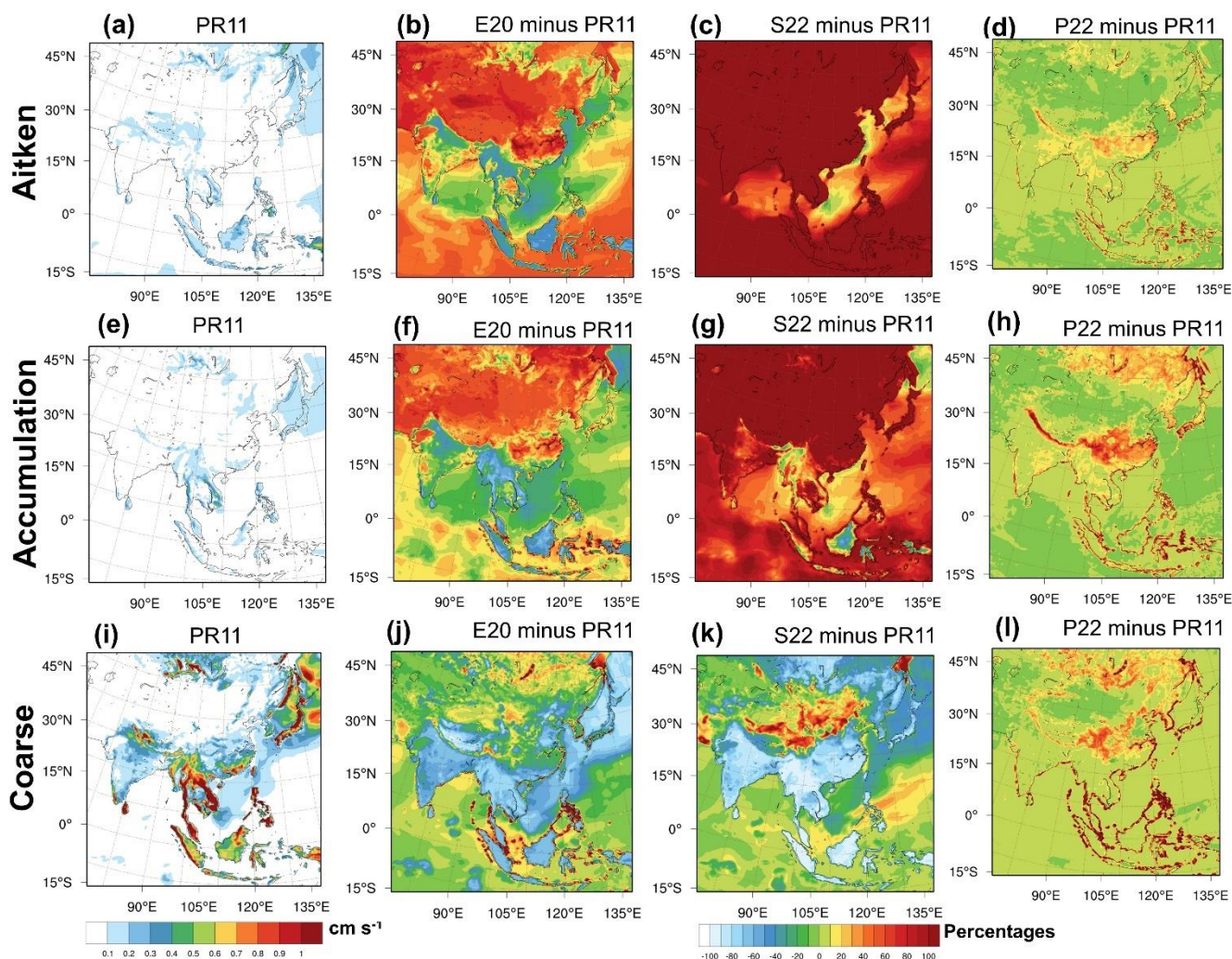


684

685 **Figure 6:** 10-days averaged dry  $V_d$  predicted by CMAQv5.4 for the Aitken, accumulation, and coarse  
686 particle modes using the PR11(blue), E20(red), S22(green) and P22(purple) particle dry deposition  
687 schemes. The variability illustrated by the boxes and whiskers corresponds to spatial variability in  
688 annually averaged values throughout the CMAQ domain.

689

690



691

692 **Figure 7:** CMAQ estimated 10 days (22-31 January 2023) averaged for the (a-d) Aitken, (e-h)  
693 accumulation, and (i-l) coarse particle modes for PR11 dry deposition scheme (a, e, i) and the  
694 corresponding concentration percentage changes (%) using (b, f, j) E20, (c, g, k) S22 and (d, h, l) P22  
695 schemes.

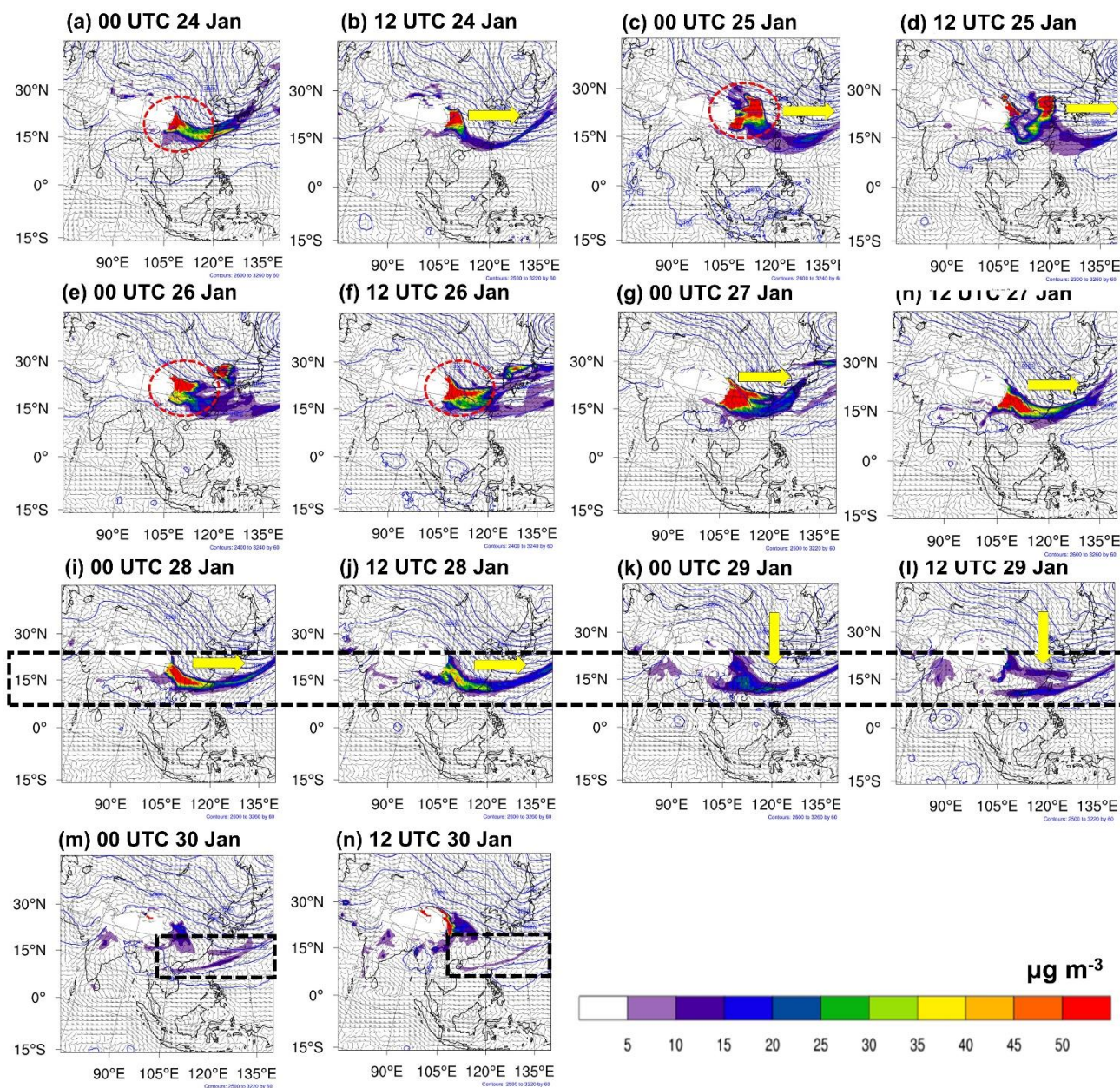
696

697

698

699

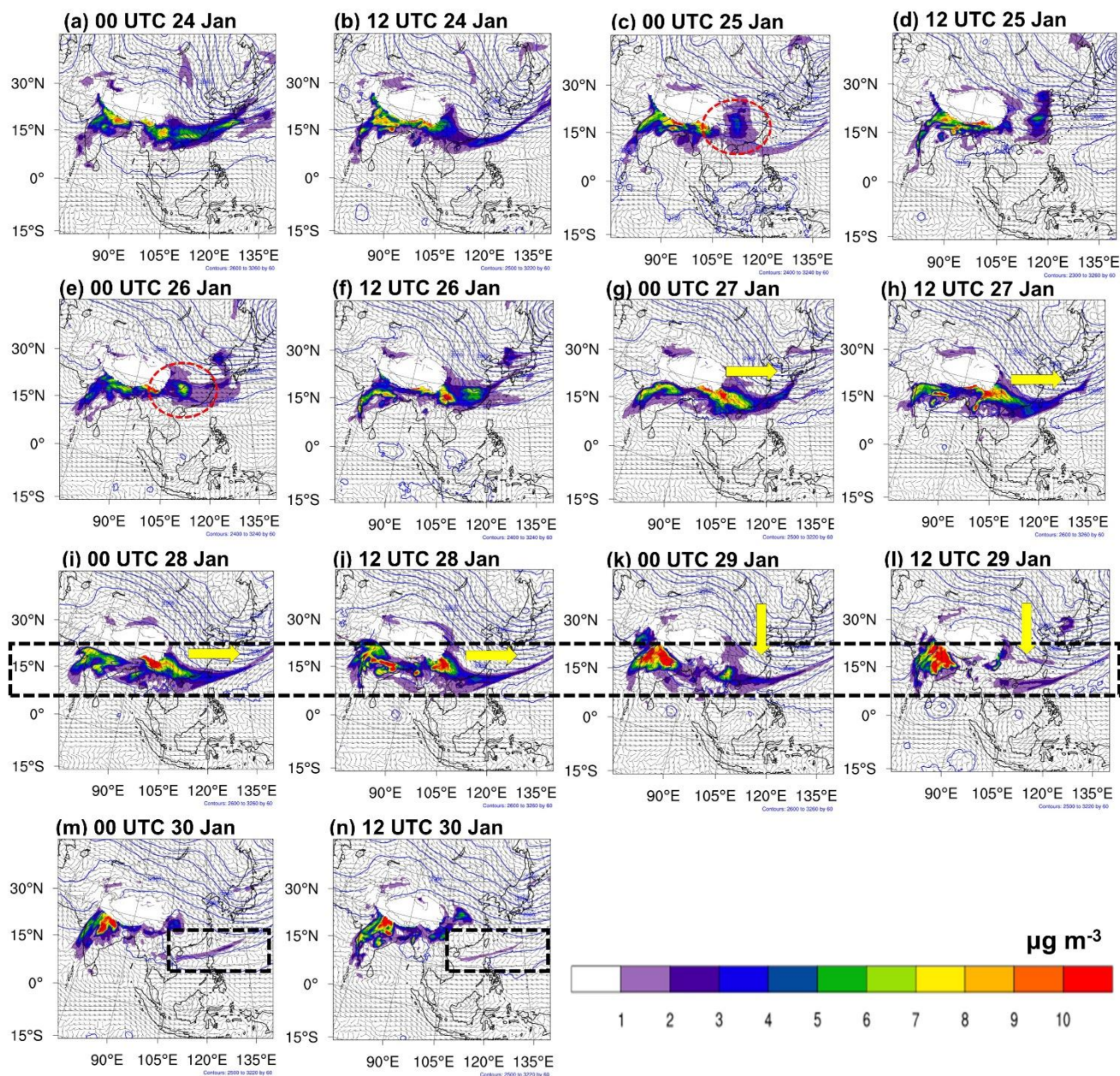




700

701 **Figure 8:** CMAQ mineral dust aerosol concentration at the 700 hPa during 24-30 January 2023. The  
702 yellow arrows highlight the trough moving direction. The dash-black rectangular box highlights the dust  
703 belt.

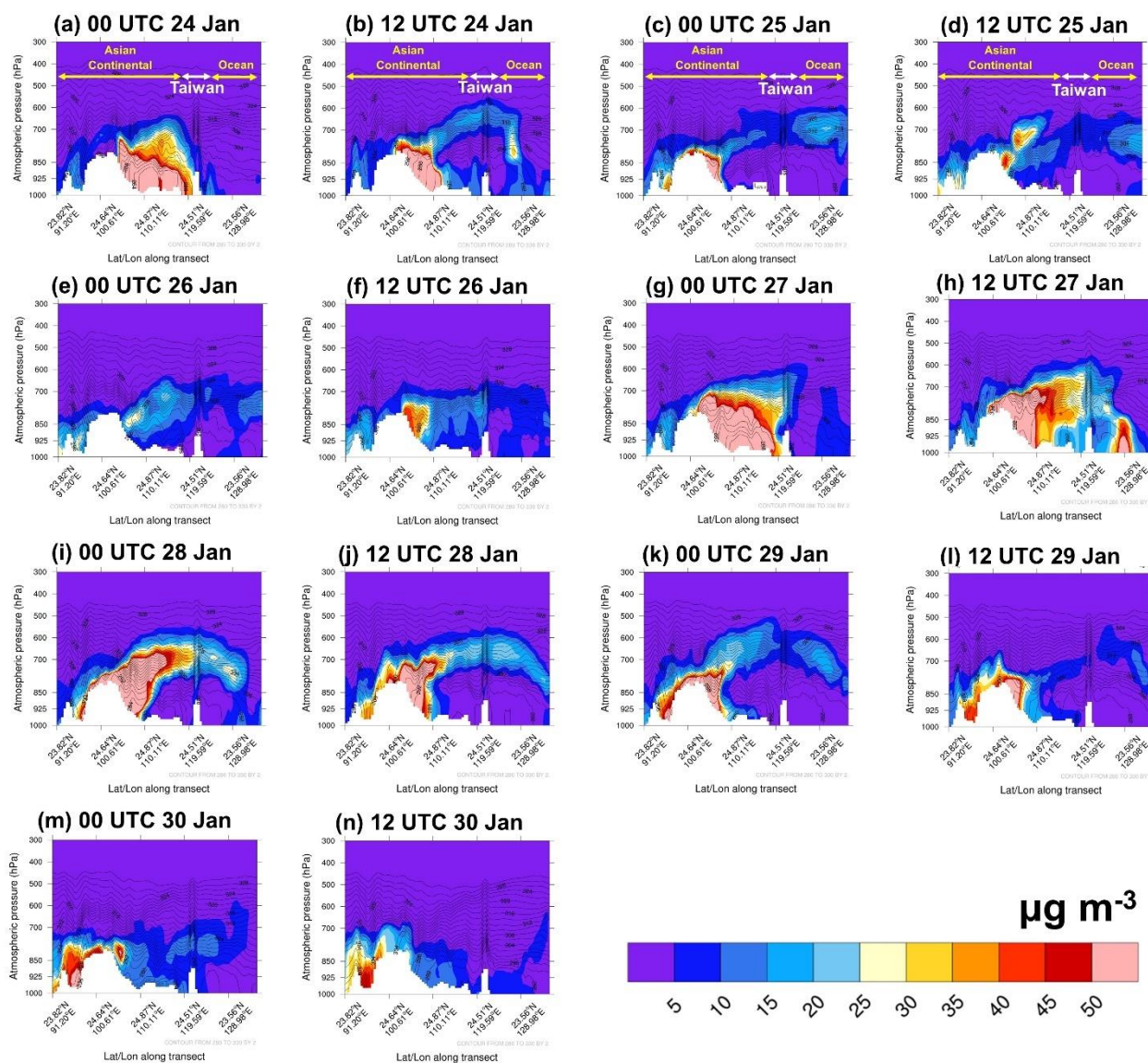
704



705

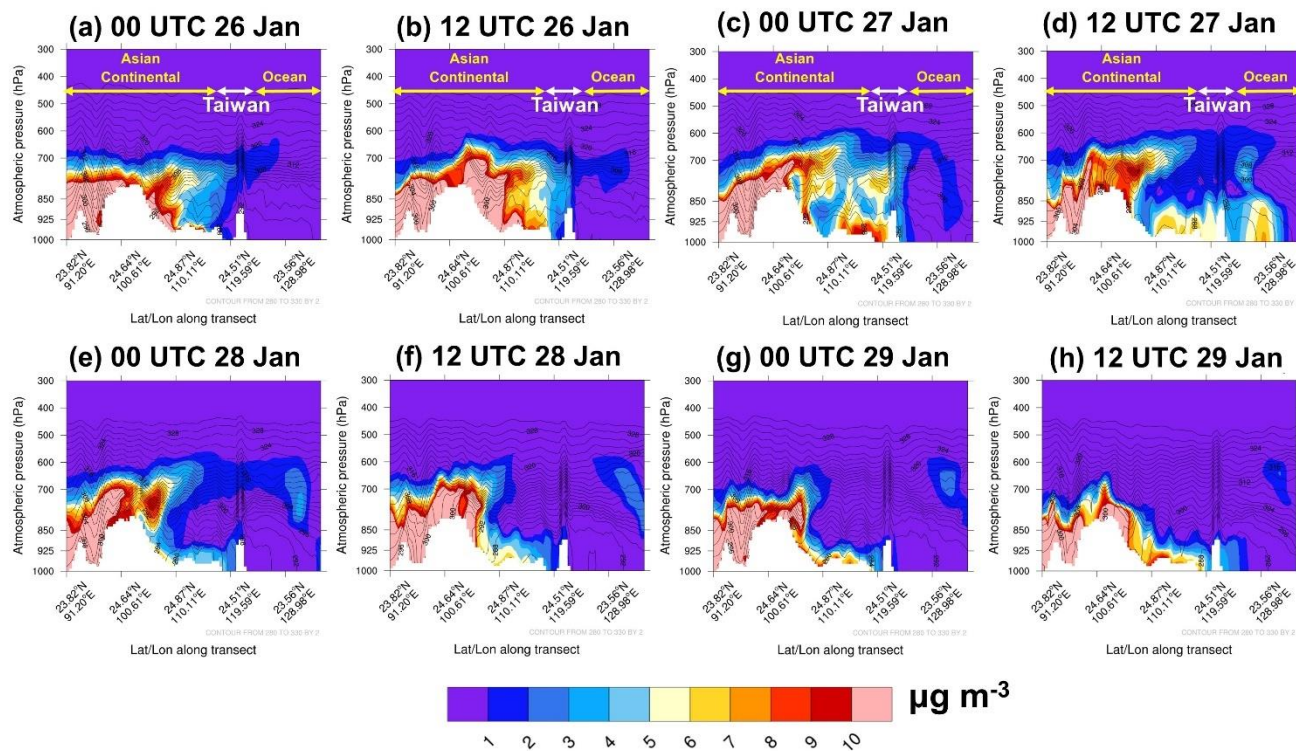
706 **Figure 9:** CMAQ black carbon concentration at the 700 hPa during 24-30 January 2023. The yellow  
707 arrows highlight the trough moving direction. The dash-black rectangular box highlights the dust belt.

708



709  
 710 **Figure 10:** Vertical profile of simulated dust aerosol for the CMAQ simulation during 24-30 January  
 711 2023.

712  
 713  
 714  
 715



716

717 **Figure 11:** Vertical profile of simulated black carbon aerosol for the CMAQ simulation during 26-29  
718 January 2023.

719

720

721

722

723

724

725

726

727

728